https://dx.doi.org/10.1016/j.engstruct.2019.04.057
This is the Pre-Published Version.

PAprC18

Modelling Tensile Tests on High Strength S690 Steel Materials undergoing Large Deformations

Ho H.C.[1,2], Chung K.F. [1,2*], Liu X.[1,2], Xiao M.[1,2], and Nethercot, D.A.[1,3]

[1] Department of Civil and Environmental Engineering,
[2] Chinese National Engineering Research Centre for Steel Construction (Hong Kong Branch),
The Hong Kong Polytechnic University, Hong Kong SAR, China
[3]The Imperial College London, U.K.
*****Corresponding author: kwok-fai.chung@polyu.edu.hk

ABSTRACT

Standard tensile tests are commonly used to determine mechanical properties of metallic materials, such as yield strength ad tensile strength as well as ductility. In general, these standard tensile tests are able to provide basic mechanical properties of steel materials, commonly referred as engineering stress-strain curves. These curves are considered to be effective for linear elastic and post yielding deformations up to mobilization of tensile strengths, and they are widely adopted in structural design and analysis of steel structures. However, for detailed investigations into structural behaviour of steel structures in large deformations beyond onset of necking, cross-sectional changes in the steel materials often become very large. Hence, an improved stress-strain curve, commonly known as a true stress-strain curve, with proper adjustment according to large longitudinal deformations should be adopted in advanced finite element models.

In order to develop full range true stress-strain curves of various steel materials for large deformations, a research project is conducted to perform an integrated experimental and numerical study. Standard tensile tests on two S275 steel coupons and two S690 steel coupons are carried out, and advanced optical measurements using a digital imaging correlation technique are adopted to measure deformation fields of these coupons with a high precision during the entire deformation ranges. After data analyses using three different transformation rules, namely, i) Power Law Method, ii) Linear Law Method, and iii) Instantaneous Area Method, three different true stress-strain curves for each of S275 and S690 steel materials are derived. These curves are then incorporated into advanced finite element models to simulate large deformations of these steel coupons observed in the tensile tests. Improvements to the true stress-strain curves derived from Instantaneous Area Method are made through successive corrections according to measured and predicted deformation characteristics of the steel coupons. Consequently, the proposed true stress-strain curves determined with Instantaneous Area Method are shown to be highly acceptable for numerical analyses of steel structures undergoing large plastic deformations up to fracture. Expressions of the proposed full range true stress-strain curves for S275 and S690 steel materials are also provided.

© 2019. This manuscript version is made available under the CC-BY-NC-ND 4.0 license http://creativecommons.org/licenses/by-nc-nd/4.0/

Keywords: High strength steel; true stress-strain curves; tensile tests; large deformations; finite element modelling; precision measurements.

1. INTRODUCTION

In general, high strength S690 steel materials are manufactured with the process of quenching and tempering (Q&T) so that their microstructures are very different to those of S275 and S355 steel materials in achieving increased strengths at an expense of ductility. Hence, the stress-strain curves of the S690 steel materials are quite different from those of the S275 and the S355 steel materials. Tensile tests are commonly used to determine mechanical properties of metallic materials, such as yield strengths, tensile strengths and ductility. In order to allow for effective comparison on test results, specific details of the standard tensile tests have been formulated, and these include i) shapes and sizes of steel coupons, ii) straining rates, iii) methods of measurements, and iv) data analysis, etc. Both ASTM E8/E8M-13 [1] and EN ISO 6892-1 [2] provide full descriptions on testing methods and procedures in conducting tensile tests on metallic materials under ambient temperature, and they are able to determine basic mechanical properties of steel materials, commonly referred as engineering stress-strain (σ_e - ε_e) curves.

Owing to different delivery conditions, steel materials are found to have different engineering stress-strain (σ_e - ε_e) curves [5] (Willms 2009). As shown in Figure 1, the following three models have been widely adopted for numerical modelling of steel structures [6, 7] (Dasilva and Coelho 2001, Shi et al 2012):

i) an elastro-perfectly plastic model;
ii) an elastro-plastic bi-linear model; and
iii) an elastro-plastic tri-linear model.

In general, these simplified models are good for numerical simulation of steel structures undergoing deformations up to a strain at about 5%. However, for detailed investigations into structural behaviour of steel structures undergoing large deformations beyond on-set of necking, cross-sectional changes in the steel materials often become very large. Hence, an improved stress-strain curve, commonly known as a true stress-strain (σ_t - ε_t) curve, with proper adjustment for occurrence of necking, should be adopted in advanced finite element modelling of steel structures undergoing large deformations.

1.1. Prediction of true stress-strain curves

Accurate true stress-strain (σ_t - ε_t) curves are essential for effective numerical investigations into structural behaviour of steel structures undergoing large deformations, typically found in structures under extreme loadings, structural members exhibiting inelastic behaviour and significant strain hardening at joints, and modelling of bolted connections. Over the past twenty years, many researchers in material mechanics and structural engineering developed various empirical transformation methods to derive the true stress-strain curves based on measured engineering stress-strain curves. Currently, the true stress-strain curves of the steel materials are determined using either analytical methods or semi-empirical methods [8, 9] as there is a lack of accurately measured data of true stresses and strains of the steel coupons during standard tensile tests. The most widely adopted transformation method to give a true stress-strain (σ_t - ε_t) curve from an engineering stress-strain (σ_e - ε_e) curve is shown as follows:

- Model TSS: Integration method

  This is an analytical method [10] (Bridgeman 1952) derived from integrating strains of a deformed steel coupon, and it is assumed that the volume of the steel material remains constant throughout the entire deformation history. The corresponding true stress-strain curve is given by:

$$\varepsilon_t = \ln (1 + \varepsilon_e) \quad (1)$$

$$\sigma_t = \sigma_e (1 + \varepsilon_e) \quad (2)$$

  where

  ε_e is the engineering strain,
  ε_t is the true strain,
  σ_e is the engineering stress, and
  σ_t is the true stress.

  This method is widely adopted because of its simplicity, and measurements on the original geometry as well as both the applied force and the tensile strains of the steel coupon are readily achieved. It should be noted that formulation of this method assumes a uniform deformation throughout the gauge length of the steel coupon. Hence, this method is readily applicable to predict deformations in the steel coupon up to on-set of necking, i.e. occurrence of highly localized deformations within the gauge length of the steel coupon, leading to mobilization of the tensile strength of the steel material.

In order to extend the stress-strain curves to cover deformations after onset of necking of the steel material, the following two widely adopted transformation methods are described:

- Model TSS-1: Power law method

  This method [10, 11] (Bridgman, 1952; Zhang and Li, 1994) adopts a high order empirical expression to define true stress, σ_t , in term of engineering strain, σ_e , after onset of necking of the steel material. It may be considered as an extension to Model TSS Integration method [10] as follows:

  $$\sigma_t = K \varepsilon_t^N \quad (3)$$

  where

  N is equal to the true strain, $\varepsilon_{t,u}$, corresponding to the tensile strength,
  K = $\sigma_{t,u} / N^N$,
  $\varepsilon_{t,u}$ is the true strain at the onset of necking, and
  $\sigma_{t,u}$ is the true tensile strength.

- Model TSS-2: Linear law method

  This method [8, 10] adopts the following empirical correction expression:

  $$\sigma_t = a + b \varepsilon_t \quad (4)$$

  where

  a = $\sigma_{t,u} (1 - \varepsilon_{t,u})$, and
  b = $\sigma_{t,u}$

Both Equations (3) and (4) are considered as extrapolation methods used to predict the true stress-strain curve beyond onset of necking, i.e. after mobilization of the tensile strength of the steel material. It should be noted that application of the proposed stress-strain curves in structural analyses of steel members or sections up to fracture is allowed though accuracy is somehow uncertain because of a lack of test data.

1.2. Objectives and scope of work

In order to promote effective use of high strength S690 steel materials in construction, a comprehensive research programme into structural performance of high strength S690 steel sections was undertaken by the authors since 2011. Extensive experimental and numerical investigations into structural behaviour of high strength S690 welded H-sections and I-sections were conducted, and supplementary design rules in accordance with EN 1993-1-1 were developed for a) section classifications, b) both stocky and slender columns under i) compression, and ii) combined compression and bending, and c) both partially restrained and unrestrained beams undergoing lateral torsional buckling. Large deformations in these high strength S690 steel materials were often encountered.

This paper presents an integrated experimental and numerical investigation to formulate full range true stress-strain (σ_t - ε_t) curves of both S275 and S690 steel materials. The investigation consists of the following tasks:

a) To conduct standard tensile tests on coupons of both the steel materials with rectangular cross-sections, and precision measurements are made to obtain instantaneous dimensions of the steel coupons during testing.

b) To derive true stress-strain (σ_t - ε_t) curves for both the steel materials through the use of various transformation methods.

c) To establish advanced finite element models to simulate standard tensile tests, and to predict load-extension (N - δ)$_p$ curves of those tests conducted in item a) above.

d) To modify true stress-strain (σ_t - ε_t) curves for both the steel materials based on high precision measurements in order to improve accuracy of the predicted load-extension (N - δ) curves of those tests conducted in item a) above.

A total of four standard tensile tests were carried out, and deformation fields over the gauge lengths were measured continuously with the use of a digital imaging correlation technique during the entire deformation history. Advanced finite element models with material and geometrical non-linearity using various true stress-strain curves were established and calibrated carefully against test results. The areas of interest in this investigation include:

- deformation characteristics of the steel coupons beyond onset of necking, but up to fracture;
- instantaneous dimensions at the critical cross-section with a minimum cross-sectional area; and
- non-uniform stress and strain distributions across critical cross-sections of the steel coupons.

It should be noted that through this integrated experimental and numerical investigation, a mechanism to derive corrected true stress-strain curves based on measured instantaneous dimensions for accurate prediction of both the S275 and the S690 steel materials at large deformations up to fracture is achieved.

2. EXPERIMENTAL INVESTIGATION

A total of four standard tensile tests were carried out according to BS EN ISO 6892-1 (2009) [2] to determine basic mechanical properties of the S275 and the S690 steel materials, and Table 1 summarizes details of the test programme. Figure 2 illustrates typical geometry of the steel coupons, and it should be noted that coupons with a rectangular cross-section of 10 x 6 mm are adopted in all these four tests. Typical test setup is shown in Figure 3. In addition to the use of a pair of strain gauges

in each steel coupon, an optical precision measurement system using the digital imaging correlation technique is also employed to measure strain fields within the gauge lengths of the steel coupons throughout the entire deformation history. It should be noted that strain gauges of Model YFLA5 and adhesive of Model CN-Y of Tokyo Sokki Kenkyujo are adopted, and this allows reliable and accurate measurements of strains up to 20% to be made. Moreover, forces are carefully applied through a displacement control to the coupons so that the straining rates are sufficiently small to avoid any dynamic effect.

2.1 Test results

All these four standard tensile tests have been conducted successfully, and Figure 4 plots all the load-extension (N - δ) curves of the four tests onto the same graph for direct comparison. It is evident that for each steel material, the two load-extension (N - δ) curves agree with each other very well throughout their entire deformation history. Table 2 summarizes key results of the standard tensile tests, and hence, the basic mechanical properties of both the S275 and the S690 steel materials. The corresponding engineering stress-strain (σ_e - ε_e) curves of the S275 and the S690 steel coupons based on the deformations within the overall gauge lengths are presented in Figure 5. It should be noted that these curves are determined with the following:

i) strain gauges up to engineering strains at about 20% and 8% for the S275 and the S690 steel materials respectively, and

ii) the digital imaging correlation technique up to fracture at engineering strains of about 45% and 14% for the S275 and the S690 steel materials respectively.

In general, the values of engineering strains measured with the strain gauges are found to follow closely to those measured with the digital imaging correlation technique.

2.2 Instantaneous deformations and dimensions of the steel coupons

Deformations and measured strain fields recorded using the digital imaging correlation technique at specific deformation stages of the standard tensile tests during the entire deformation history are illustrated in Figures 6 and 7 for the S275 and the S690 steel materials respectively. It is apparent that the strain fields at low stresses are fairly uniform along the gauge lengths of the steel coupons. However, once necking occurs, highly localized surface strains occur in the close vicinity of the cross-section undergoing necking, i.e. the critical cross-section with a minimum cross-sectional area. It

should be noted that the maximum true strains ε_t at the critical cross-sections are found to be 147% and 89% in the S275 and the S690 steel coupons respectively.

Based on the measured instantaneous dimensions of the critical cross-sections of the S275 and the S690 steel coupons, their instantaneous cross-sectional areas, A_i, under the corresponding engineering strain, ε_e, are plotted in Figure 8a). In order to compare this necking phenomena of the two steel coupons, two parameters are introduced as follows:

- Normalized ratio of instantaneous area, $\varphi_{A_i} = {A_i}/{A_0}$; (5)
- Normalized ratio of engineering strain, $\varphi_\varepsilon = {\varepsilon_i}/{\varepsilon_u}$ (6)

where A_i is the instantaneous cross-sectional area;
A_0 is the initial cross-sectional area;

ε_i is the instantaneous engineering strain;
ε_u is the engineering strain corresponding to the point of tensile strength.

Figure 8b plots variations of the normalized ratio of instantaneous area, φ_{A_i}, against the normalized ratio of engineering strain φ_ε. It should be noted that φ_{A_i} is equal to 1.0 at the initial state at which φ_ε is equal to zero. When φ_ε is equal to 1.0, the normalized instantaneous areas, φ_{A_i} are reduced to 0.92 and 0.80 for the S275 and the S690 steel materials respectively. It is interesting to note that fracture takes place when the value of φ_ε reachs about 2.2 while the corresponding value of φ_{Ai} is close to 0.4 for both steel materials. Typical failure modes of these steel coupons after fracture are shown in Figure 9, and all the steel coupons are found to fail in tension with fracture initiated from their cores, and then with significant shearing in the surrounding materials.

2.3 Measured and predicted true stress-strain curves

Owing to the use of the digital imaging correlation technique, instantaneous dimensions of the critical cross-sections of the steel coupons are continuously measured throughout the entire deformation history. Hence, it is considered to be appropriate to propose a new transformation method, namely, Model TSS-3: Instantaneous area method, which is able to provide a full-range true stress-strain $(\sigma_t - \varepsilon_t)_m$ curve based on measured instantaneous dimensions of the steel coupons. Hence, the transformation method is given as follows:

- Model TSS-3: Instantaneous area method

  Based on the assumption of constant volume in the steel coupons under large deformations, both the true stress, σ_t , and the true strain, ε_t , after on-set of necking, are given as follows:

$$\varepsilon_t = \eta_\varepsilon \ln (A_o / A_i) \quad (7)$$

$$\sigma_t = \eta_\sigma . N_i / A_i \quad (8)$$

where

A_o is the original cross-sectional area ;
A_i is the measured instantaneous cross-sectional area ;
N_i is the applied force corresponding to A_i ;
η_ε is a correction factor due to a non-uniform strain distribution within the cross section of the steel coupon ; and
η_σ is a correction factor due to a non-uniform stress distribution within the cross section of the steel coupon.

It should be noted that the values of both η_σ and η_ε may be taken as 1.0 initially, and they will be refined after comparison with measured data through iterations. Refer to Section 3.4 for further details of these two correction factors.

Through the use of the instantaneous dimensions of the steel coupons, the measured true stress-strain $(\sigma_t - \varepsilon_t)_m$ curves of the S275 and the S690 steel materials together with those predicted true stress-strain $(\sigma_t - \varepsilon_t)_p$ curves derived with the transformation methods of Models TSS-1, TSS-2 and TSS-3 are plotted onto the same graph in Figure 10 for direct comparison. It is shown that

- for the S275 steel materials, the predicted true stress-strain $(\sigma_t - \varepsilon_t)_p$ curves derived from Models TSS-2 and TSS-3 are very close to the measured true stress-strain $(\sigma_t - \varepsilon_t)_m$ curve, when compared with that derived from Model TSS-1;
- However, the predicted true stress-strain $(\sigma_t - \varepsilon_t)_p$ curves derived from Models TSS-1 and TSS-3 for the S690 steel materials are close to the measured true stress-strain $(\sigma_t - \varepsilon_t)_m$ curve, when compared with derived from Model TSS-2.

Therefore, it is shown that only the transformation method of Model TSS-3 for true stress-strain $(\sigma_t - \varepsilon_t)_p$ curves are likely to be able to provide good results, when compared with the measured true stress-strain $(\sigma_t - \varepsilon_t)_m$ curves for both the S275 and the S690 steel materials. Improvements to the transformation method of Model TSS-3 will be presented in the following sections.

3. NUMERICAL INVESTIGATION

In order to simulate load-extension (N - δ) curves of the S275 and the S690 steel coupons in the standard tensile tests, advanced finite element models using ABAQUS 6.13 (2013) [12] with material and geometrical non-linearity have been established. An eight-noded solid element with reduced integration, namely, a continuum element C3D8R, is adopted, and typical mesh of the finite element

models is shown in Figure 11. Local mesh refinement is provided at the mid-lengths of the finite element models in order to improve numerical accuracy of the models as these elements will be extensively sketched with significant lateral contraction after necking.

3.1 Modelling damage

In order to simulate fracture failure in the models at large deformations, a damage model is introduced into the material model of these elements in which a damage type of "Ductile fracture of metals" is adopted for simulation of a tensile fracture failure which incorporates a mechanism of void nucleation, coalescence, and growth. Hence, the following components of the material model are defined as shown in Figure 12:

i) Damage initiation: Point P
ii) Complete degradation: Point Q
iii) Damage evolution: Path PQ
iv) Degradation of elasticity

It should be noted that a post damage initiation material behaviour should be defined in a "Damage Evolution" module, which describes the rate of degradation of the Young's modulus of the steel materials after damage initiation. The expression for a damaged stress, σ_d, is based on the following scalar damage approach:

$$\sigma_d = (1 - D)\,\bar{\sigma} \qquad (9)$$

where D is a damage variable ranging from 0 to 1; and
$\bar{\sigma}$ is the stress without any damage in the steel material.

Moreover, a linear softening approach is adopted for damage evolution modelling using an effective plastic strain, $\varepsilon_{t,f1} - \varepsilon_{t,f}$, at 0.02. A graphical presentation of this damage evolution modelling is shown in Figure 12.

3.2 Convergence study

It is essential to demonstrate numerical convergence of the finite element models, and hence, a total of three meshes with different element sizes are established, namely Meshes M1, M2 and M3. The programme of convergence study is summarized in Table 3. Material and geometrical non-linear analyses of all these models have been completed successfully while the key results are presented in Table 3 for easy comparison. It is shown in Figure 13 that these three finite element models with different meshes are able to predict the load-extension $(N - \delta)_p$ curves of the steel coupon satisfactorily, and Mesh M2 is able to achieve a high numerical accuracy with an optimal computing time. Hence,

Mesh M2 is adopted for subsequent numerical analyses. The deformed shape of Mesh M2 at various deformation stages, namely, "Stage I - initiate state", "Stage Y – onset of yielding", "Stage N - onset of necking", and "Stage F - fracture initiation", are illustrated in Figure 14.

3.3 Numerical results

Figure 15 plots the load-extension $(N - \delta)_p$ curves of the finite element models of the standard tensile tests incorporating the predicted true stress-strain $(\sigma_t - \varepsilon_t)_p$ curves of Models TSS-1 and TSS-2 for both the S275 and the S690 steel materials. It is evident that

i) the predicted load-extension $(N - \delta)_p$ curves derived from these two finite elements models deviate significantly from the measured $(N - \delta)_m$ curves of both steel materials after utilization of the maximum resistances of the steel coupons;
ii) the predicted load-extension $(N - \delta)_p$ curves derived from Model TSS-2 is close to the measured $(N - \delta)_m$ curves for the S275 steel coupon, and
iii) the predicted load-extension $(N - \delta)_p$ curves derived from Model TSS-1 is close to the measured $(N - \delta)_m$ curves for the S690 steel coupon.

3.4 Non-uniform stress and strain distributions within critical cross-sections

It should be noted that the strain measured with the use of the digital image correlation (DIC) technique are surface strains of the steel coupons, and they are the lowest strains across the critical cross-sections. It is possible to examine the internal "stress and strain" conditions using the finite element models. Figures 16 and 17 illustrate the stress and strain distributions within the critical cross-sections at various deformation states for both the S275 and the S690 steel coupons. It is shown that

a) the stresses are evenly distributed within the critical cross-section from the initial state to the yield state, i.e. Stages I and Y, as well as up to mobilization of the tensile strength, i.e. Stage N;

b) at large deformations after onset of necking i.e. Stages NF1, NF2, NF3 and F, both the stresses and the strains become uneven within the critical cross-sections, and hence, the stresses over the cores of the cross-sections are always larger than those towards both edges of the cross-sections;

c) for the S275 steel coupons, the maximum stress at the centre of the critical cross-sections is found to be 2,392 N/mm^2 at Stage F while the stress at the edges of the critical cross-sections is found to be merely 2,008 N/mm^2, and hence, the ratio of these two values is 1.19;

d) for the S690 steel coupons, the maximum stress at the centre of the critical cross-section is found to be 1,387 N/mm^2 at Stage F while the stress at the edges of the critical cross-sections is found to be merely 969 N/mm^2, and hence, the ratio of these two values is 1.43.

A close examination into the data analyses of the tensile tests reveals that such effect of non-uniformity has not been considered during determination of the measured engineering as well as the measured true stresses and strains. This leads to a systematic under-estimation to the true stresses of the steel materials determined at the critical cross-sections after onset of necking. Key results of the finite element modelling of the S275 and the S690 steel coupons are summarized in Tables 4 and 5 respectively.

3.4.1 Correction factors for non-uniform stress and strain distributions

In order to quantify variations of both the stress and the strain distributions across the critical cross-sections at various strain levels, two parameters, namely a stress correction factor, η_σ , and a strain correction factor, η_ε, are introduced, which are defined as follows:

$$\eta_\sigma = \frac{\sigma_{vm,max}}{\sigma_{av}} \quad (10)$$

$$\eta_\varepsilon = \frac{\varepsilon_{tp,max}}{\varepsilon_{av}} \quad (11)$$

$$\sigma_{vm,max} = \frac{1}{\sqrt{2}}\left[(\sigma_x - \sigma_y)^2 + (\sigma_y - \sigma_z)^2 + (\sigma_z - \sigma_x)^2 + 6(\tau_{xy}{}^2 + \tau_{yz}{}^2 + \tau_{zx}{}^2)\right]^{1/2} \quad (12)$$

where $\sigma_{vm,max}$ is the maximum von Mises stress of the critical cross-section;
$\varepsilon_{tp,max}$ is the maximum principal true strain of the critical cross-section;
σ_{av} is the average tensile stress within the critical cross-section; and
ε_{av} is the average tensile strain within the critical cross-section;

Figure 18 presents variations of the values of both η_σ and η_ε at various true strains after onset of necking, and it should be noted that

a) before on-set of necking, the values of η_σ and η_ε are found to range narrowly from 0.998 to 1.003 and from 0.992 to 1.004 respectively for the S275 steel coupons;
b) similarly, before on-set of necking, the values of η_σ and η_ε are found to range narrowly from 0.996 to 0.998 and from 0.987 to 1.000 respectively for the S690 steel coupons;
c) after onset of necking, the value of η_σ is found to decrease from 0.998 at Stage N to 0.723 at Stage F for the S275 steel coupons, and from 0.996 at Stage N to 0.815 at Stage F for the S690 steel coupons;

d) however, the value of η_ε is found to increase from 0.992 at Stage N to 1.050 at Stage F for the S275 steel coupons, and from 0.987 at Stage N to 1.250 at Stage F for the S690 steel coupons.

Consequently, it is essential to allow for these effects of non-uniformity in both the predicted stresses and strains within the critical cross-sections during generation of the measured true stress-strain curves. Hence, incorporation of these correction factors η_σ and η_ε to Equations (7) and (8) of Model TSS3 Instantaneous area method in generating the true stress-strain (σ_t - ε_t) curves using measured instantaneous dimensions is essential for improved predictability of the model. It should be noted that this corrected true stress-strain curve is referring to the actual stress-strain state of the core point of the critical cross section of the test coupon, rather than the averaged stress-strain state of the critical cross section of the test coupon.

3.4.2 Iterations for corrected full-range true stress-strain curves

In order to obtain a corrected full range true stress-strain (σ_t - ε_t) curve using Model TSS3 – Instantaneous area method, iterations are needed during determination of the values of correction factors η_σ and η_ε :

- The measured true stress-strain (σ_t - ε_t) curves of the steel materials are obtained initially using Model TSS3 Instantaneous area method, i.e. with Equations (7) and (8), and both the values of factors η_σ and η_ε are assigned to be equal to 1.0. These curves are then incorporated into the finite element models to predict the entire load-extension curves of the tensile tests.
- Upon successful analyses of the finite element models, by examining both the stress and the strain distributions at the critical cross-sections of the coupons, the first estimates of correction factors η_σ and η_ε are obtained. These values are then adopted into Equations (7) and (8) again to derive corrected true stress-strain (σ_t - ε_t) curves which are then incorporated into the finite element models for the second attempt in predicting the load-extension curves.
- Upon another successful analyses of the finite element models, the second estimates of corrected factors η_σ and η_ε are then obtained after examining both the stress and the strain distributions at the critical cross-sections of the coupons.
- The process repeats until the values of correction factors η_σ and η_ε become converged, i.e. the difference in the values of both η_σ and η_ε in two successive iterations is smaller than 0.01.

It should be noted that, as summarized in Table 6, the values of correction factors η_σ and η_ε are converged to 0.72 and 0.91 respectively at Stage F after the fifth iteration for the S275 coupon.

Similarly, the values of correction factors η_σ and η_ε are converged to 0.78 and 1.20 respectively at Stage F after the fourth iteration for the S690 coupon, as summarized in Table 7. Based on the converged correction factors η_σ and η_ε, both the corrected true stress-strain curves for the S275 and the S690 steel materials have been successfully obtained, as shown in Figure 10.

3.5 Modelling of standard tensile tests with various true stress-strain curves

All the true stress-strain (σ_t - ε_t) curves derived with Models TSS-1, TSS-2 and TSS-3 shown in Figure 10 are incorporated into the finite element models to predict load-extension (N - δ) curves of the steel coupons. Material and geometrical non-linear analyses of all the finite element models have been completed successfully.

Figure 19 plots the predicted load-extension $(N - \delta)_p$ curves of the three models with various true stress-strain (σ_t - ε_t) curves for both the S275 and the S690 steel coupons for direct comparison. It is shown that:

a) all the three models are able to give close predictions to the measured data of both the S275 and the S690 steel coupons up to onset of necking;
b) for the S275 steel coupons, the predicted true stress-strain $(\sigma_t - \varepsilon_t)_p$ curves for both Models TSS-1 and TSS-2 tend to under-predict the resistances of the coupons after on-set of necking;
c) for the S690 steel coupons, the predicted true stress-strain $(\sigma_t - \varepsilon_t)_p$ curves for both Models TSS-1 and TSS-2 tend to over-predict the resistances of the coupons after on-set of necking;
d) for both the S275 and the S690 steel coupons, the measured true stress-strain $(\sigma_t - \varepsilon_t)_m$ curves for Model TSS-3 with both correction factors η_σ and η_ε are able to predict the entire load-extension $(N - \delta)_p$ curves of the steel coupons with a high level of accuracy throughout the entire deformation history up to fracture.

Consequently, it is shown that Model TSS-3 Instantaneous area method is able to provide appropriate true stress-strain (σ_t - ε_t) curves for accurate prediction of the measured load-extension $(N - \delta)_m$ curves of the standard tensile tests, and the use of both correction factors η_σ and η_ε is essential to achieve such a high accuracy. It should also be highlighted that the failure mechanism initiated by a tensile fracture at the central core of the S690 steel coupon followed by a shear failure at the surrounding materials of the coupon has been successfully simulated in the finite element models, as shown in Figure 20.

3.6 Proposed constitutive models for both S275 and S690 steel materials

Based on the corrected true stress-strain curves using Model TSS3 – Instantaneous Area Method, the constitutive models of both the S275 and the S690 steel materials are proposed as follows:

- For S275 steels,

$$\sigma_t(\epsilon) \begin{cases} \sigma_t = E_s\varepsilon_t & \text{for } \varepsilon_t \le \varepsilon_y \\ \sigma_t = f_y \times \left[1 + 6.85 \times 10^{-3} \times \left({\varepsilon_t}/{\varepsilon_y} - 1\right)\right] & \text{for } \varepsilon_y < \varepsilon_t \le 10\varepsilon_y \\ \sigma_t = f_y \times \left\{1.062 + 1.082\left[\left[\left({\varepsilon_t}/{10\varepsilon_y} - 1\right) + 0.5\right]^{0.2} - 0.87\right]\right\} & \text{for } 10\varepsilon_y < \varepsilon_t \le 180\varepsilon_y \\ \sigma_t = f_y \times \left[\left(0.925 \times 10^{-3} \times {\varepsilon_t}/{\varepsilon_y}\right)^2 + 2.84 \times 10^{-3} \times {\varepsilon_t}/{\varepsilon_y} + 1.5\right] & \text{for } 180\varepsilon_y < \varepsilon_t \le 1.8 \end{cases} \quad (13)$$

where E_s = 210 kN/mm^2

- For S690 steels,

$$\sigma_t(\varepsilon) \begin{cases} \sigma_t = E_s\varepsilon_t & \text{for } \varepsilon_t \le \varepsilon_y \\ \sigma_{nt} = f_y \times \left[1 + 3 \times 10^{-3} \times \left({\varepsilon_t}/{\varepsilon_y} - 1\right)\right] & \text{for } \varepsilon_y < \varepsilon_t \le 6\varepsilon_y \\ \sigma_{nt} = f_y \times \left\{1.015 + 0.1 \times \left[1 - 0.01 \times \left(0.6\left({\varepsilon_t}/{\varepsilon_y} - 6\right) - 10\right)^2\right]\right\} & \text{for } 6\varepsilon_y < \varepsilon_t \le 15\varepsilon_y \\ \sigma_t = f_y \times \left\{1.094 + 0.1 \times \left(\frac{{\varepsilon_t}/{\varepsilon_y} - 15}{100}\right)^{0.45}\right\} & \text{for } 15\varepsilon_y < \varepsilon_t \le 130\varepsilon_y \\ \sigma_t = f_y \times \left\{1.2 - 0.09\left[\left({\varepsilon_t}/{\varepsilon_y} - 130\right)^{1.1} \Big/ 340\right]\right\} & \text{for } 130\varepsilon_y < \varepsilon_t \le 1.2 \end{cases} \quad (14)$$

4. CONCLUSIONS

In order to promote effective use of high strength S690 steel in construction, a comprehensive research programme into structural performance of high strength S690 steel sections was undertaken by the authors over the past few years. It is considered to be essential to generate accurate true stress-strain (σ_t - ε_t) curves of the S690 steel materials for accurate prediction of structural behaviour of

these steel structures undergoing large deformations up to fracture. This paper reports an integrated experimental and numerical investigation into standard tensile tests in which a mechanism to derive true stress-strain (σ_t - ε_t) curves based on measured instantaneous dimensions is achieved for accurate prediction of both the S275 and the S690 steel materials at large deformations up to fracture. It is found that:

- The two commonly adopted transformation methods, namely, Models TSS-1 Linear law method and TSS-2 Power law method, are unable to provide accurate full range true stress-strain $(\sigma_t - \varepsilon_t)_p$ curves for accurate prediction of the load-extension $(N - \delta)_p$ curves of the standard tensile tests of both the S275 and the S690 steel materials. They are found to be ineffective because of their semi-empirical formulation without calibration against test data.
- Model TSS-3 Instantaneous area method is able to provide accurate true stress-strain (σ_t - ε_t) curves for prediction of the load-extension $(N - \delta)_p$ curves of the standard tensile tests, and the use of both correction factors η_σ and η_ε is essential to achieve a high accuracy.

Hence, the proposed investigation is demonstrated to be very effective in formulating expressions of the full range true stress-strain curves for both the S275 and the S690 steel materials up to fracture. It is essential to instantaneous dimensions of the steel coupons through the use of a digital imaging correlation technique for calibration of both the finite element models and the predicted true stress-strain $(\sigma_t - \varepsilon_t)_p$ curves. The proposed true stress-strain $(\sigma_t - \varepsilon_t)_p$ curves derived from Model TSS-3 Instantaneous area method are shown to be accurate for numerical analyses of steel structures undergoing large deformations up to fracture. Expressions of the proposed full range true stress-strain curves for S275 and S690 steel materials are also provided.

ACKNOWLEDGEMENT

The project leading to publication of this paper is partially funded by the Research Grants Council of the Government of Hong Kong SAR (Project No. PolyU 5148/13E and PolyU 152194/15E) and the Research Committee of the Hong Kong Polytechnic University (Project No. RTZX). Both technical and financial support from the Chinese National Engineering Research Centre for Steel Construction (Hong Kong Branch) (Project No. 1-BBY3 & 6) of the Hong Kong Polytechnic University is also gratefully acknowledged. Special thanks go to the Nanjing Iron and Steel Company Ltd. in Nanjing for supply of high strength steel materials. Technical supports from the multi-skilled technicians of the Structural Engineering Research Laboratory of the Department of Civil and Environmental Engineering of the Hong Kong Polytechnic University are gratefully acknowledged.

REFERENCES

[1] ASTM E8/E8M-13 (2013) Standard Test Methods for Tension Testing of Metallic Materials. ASTM International. West Conshohocken, PA.

[2] BS EN ISO 6892-1 (2009). Metallic materials – Tensile testing Part 1: Method of test at room temperature. International Organization for Standardization.

[3] Huang Y and Young B. (2012). Material properties of cold-formed lean duplex stainless steel sections. *J Thin-Walled Struct.*, 54:72–81.

[4] Huang, Y and Young, B. (2014). The Art of Coupon Tests. *Journal of Constructional Steel Research*, 96(1):159-175.

[5] Willms, R. (2009). High strength steel for steel constructions. Proceedings of the Nordic Steel Construction Conference (NSCC 2009), Malmö, Sweden, September 2 - 4, 2009; pp. 597-604.

[6] Da Silva, L. S. and Coelho, A. G. (2001). A ductility model for steel connections. *Journal of Constructional Steel Research*, 57(1), 45-70.

[7] Shi, G., Liu, Z., Ban, H. Y., Zhang, Y., Shi, Y. J., and Wang, Y. Q. (2012). Tests and finite element analysis on the local buckling of 420 MPa steel equal angle columns under axial compression. *Steel & Composite Structures*, 12(1), 31-51.

[8] Ling, Y. (1996). Uniaxial true stress-strain after necking. *AMP Journal of Technology*, 5, 37-48.

[9] Yun, X., Gardner, L. (2017). Stress-strain curves for hot-rolled steels., *Journal of Constructional Steel Research*, 133(1):36-46.

[10] Bridgeman, P. W. (1952). Studies in Large Plastic Flow and Fracture, McGraw-Hill, New York.

[11] Zhang K.S. and Li Z.H. (1994). Numerical analysis of the stress-strain curve and fracture initiation for ductile material, *Engng. Fracture Mech.*, 49:235-241.

[12] Abaqus User's Manual. Version 6.13-4 (2013). Dassault Systèmes Corp. Providence, RI, USA.

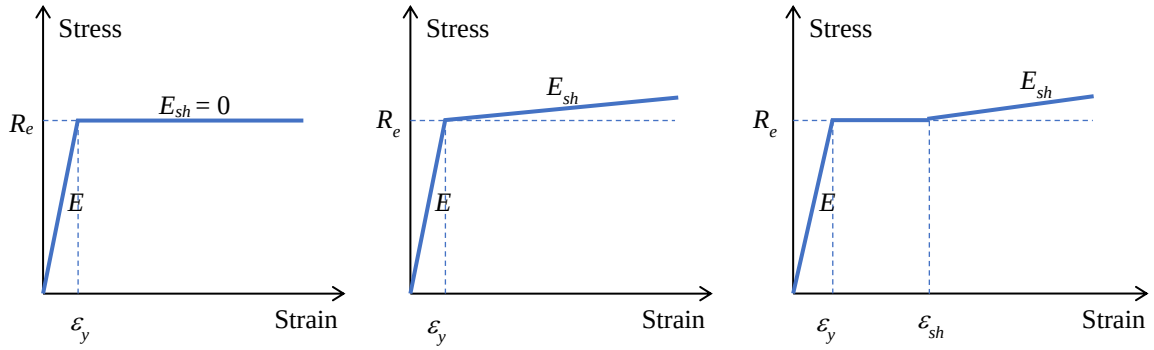

a) Elastic-perfectly plastic model

b) Elastro-plastic bi-linear model

c) Elastro-plastic tri-linear model

Figure 1: Typical simplified stress-strain curves of steel materials

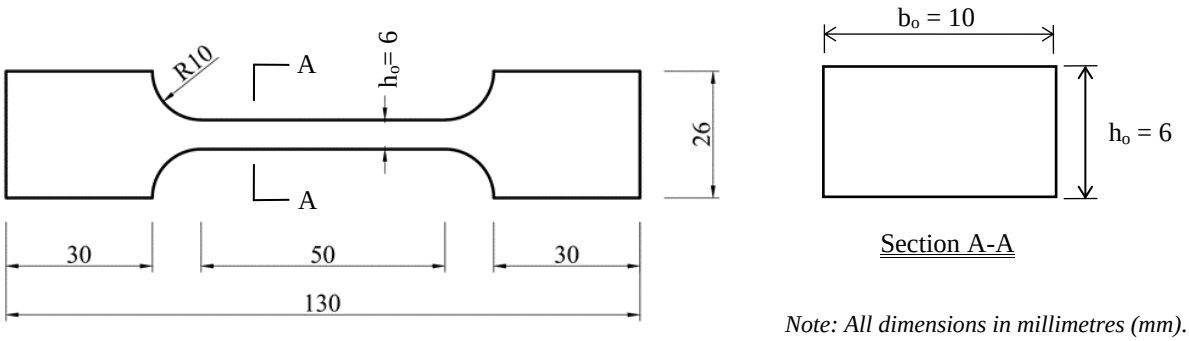

Note: All dimensions in millimetres (mm).

Figure 2: Geometry and dimensions of steel coupons

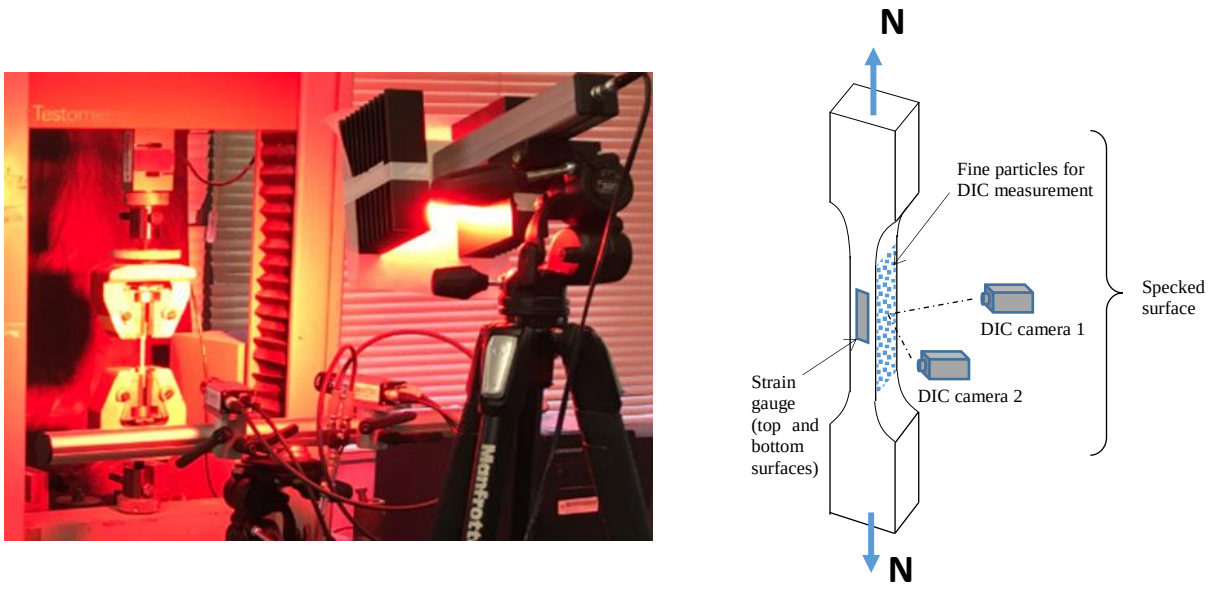

a) Test set-up with a digital image correlation system

b) Strain field measurement by i) two strain gauges and ii) a digital image correlation system

Figure 3: Typical set-up of standard tensile tests with high precision measurement

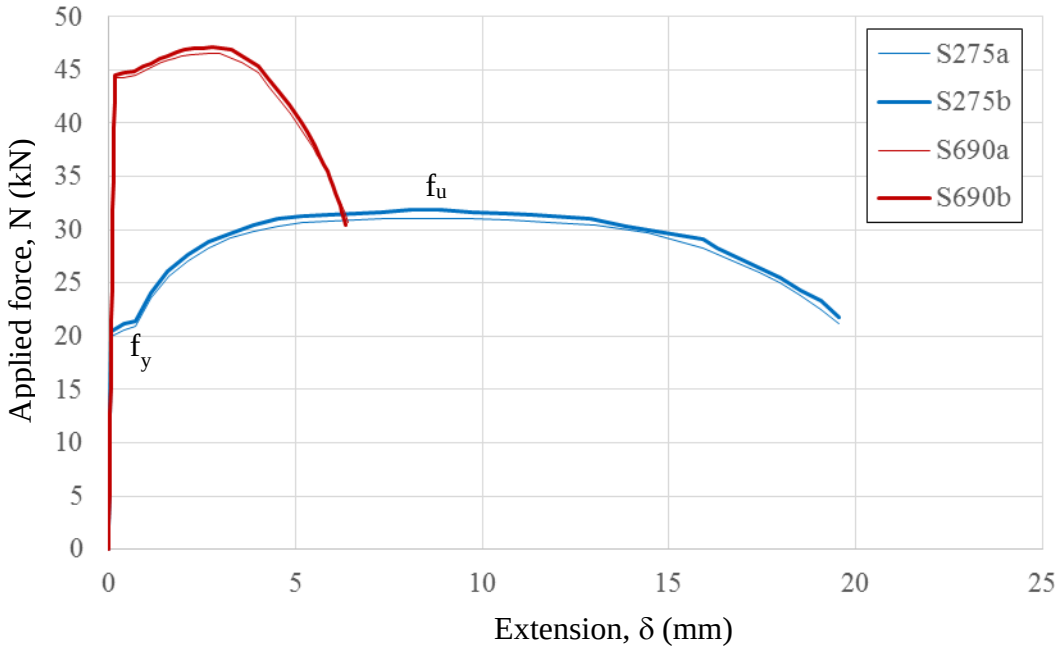

Figure 4: Load-extension curves of S275 and S690 steel coupons

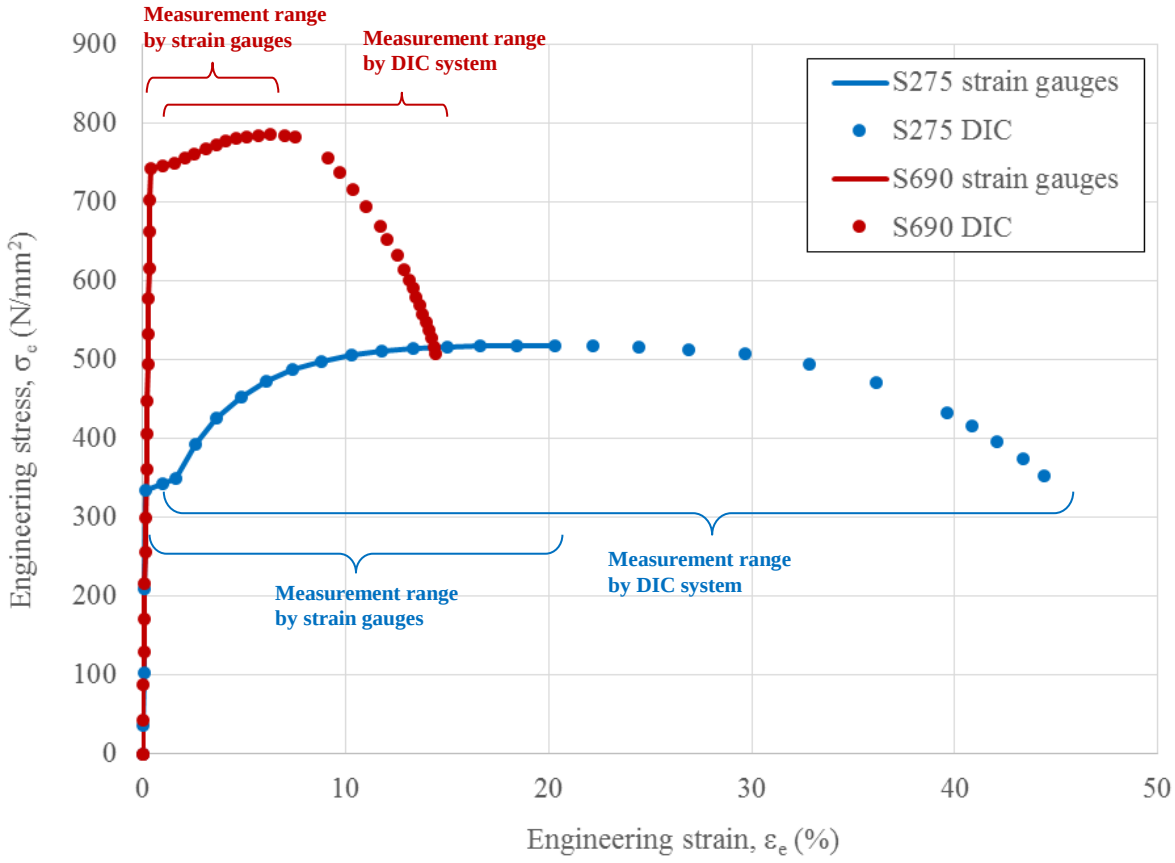

Figure 5: Engineering stress-strain curves of S275 and S690 steel coupons

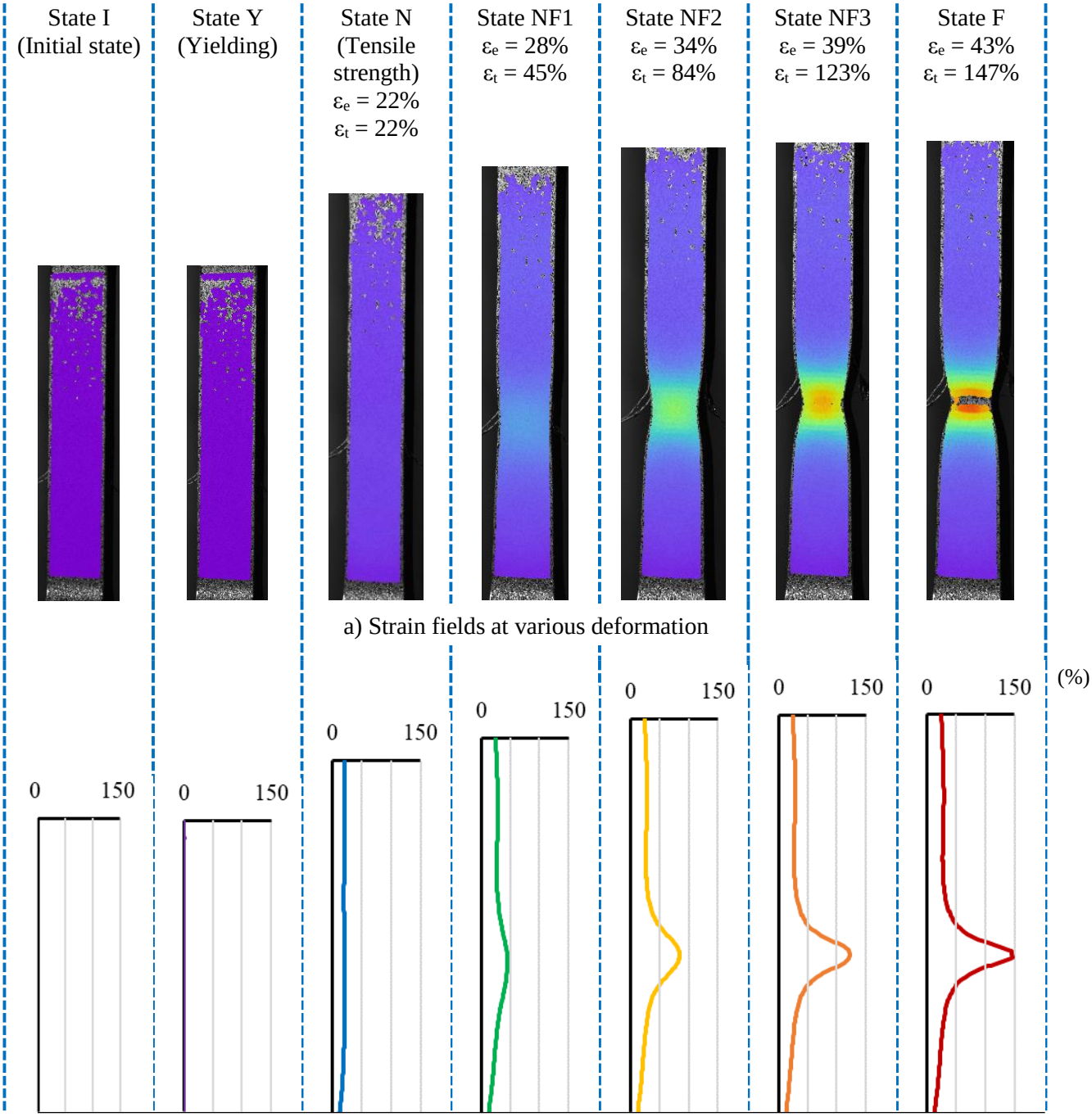

Figure 6: Typical variations of strain fields during the entire deformation history of a S275 steel coupon

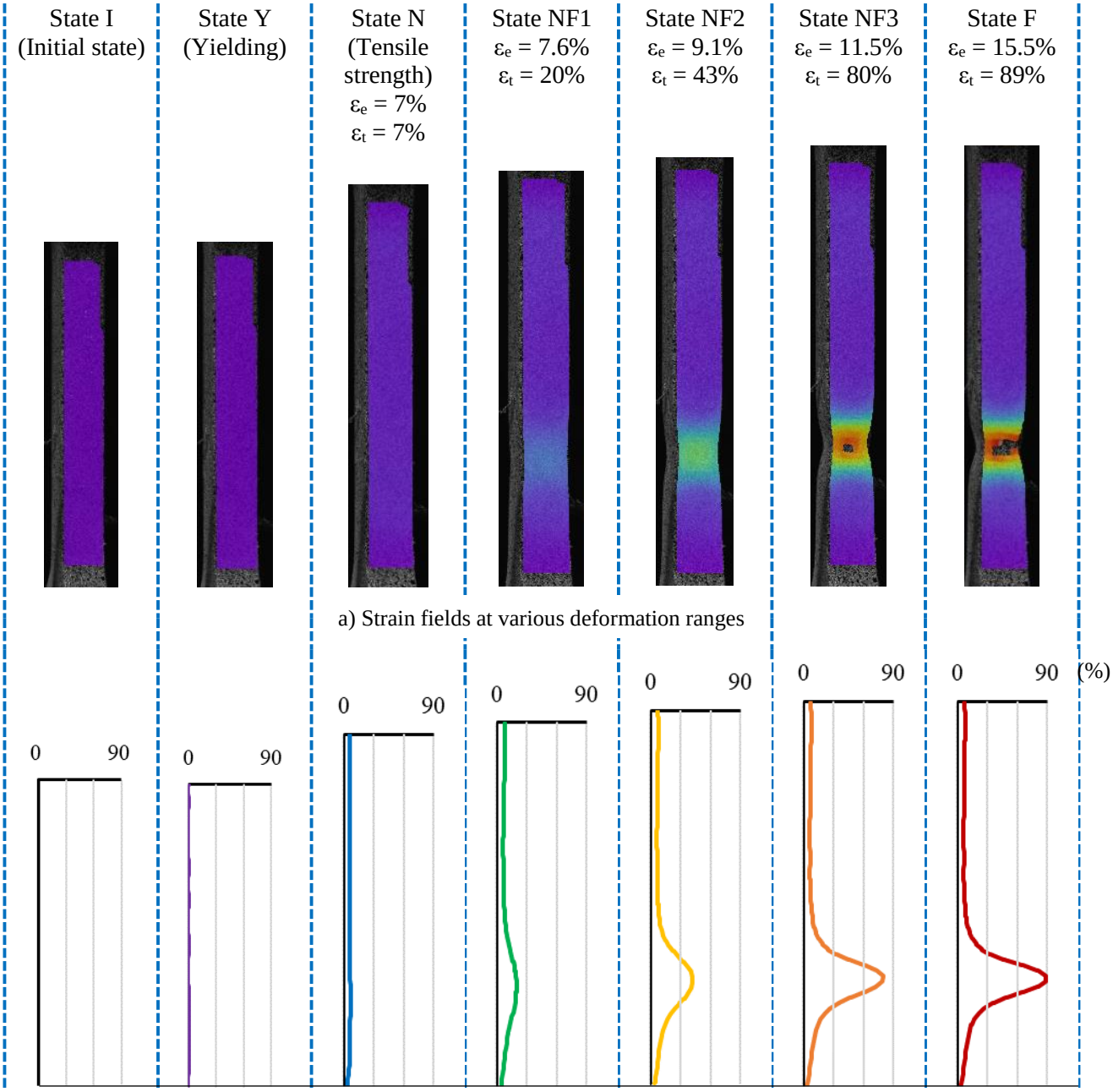

a) Strain fields at various deformation ranges

b) Strain distribution along the gauge length

Figure 7: Typical variations of strain fields during the entire deformation history of a S690 steel coupon

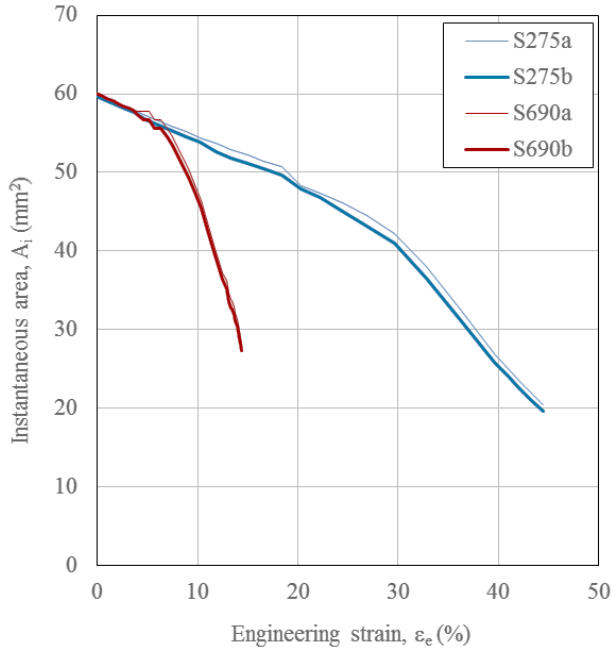

a) Variation of instantaneous area A_i against engineering strain ε_e

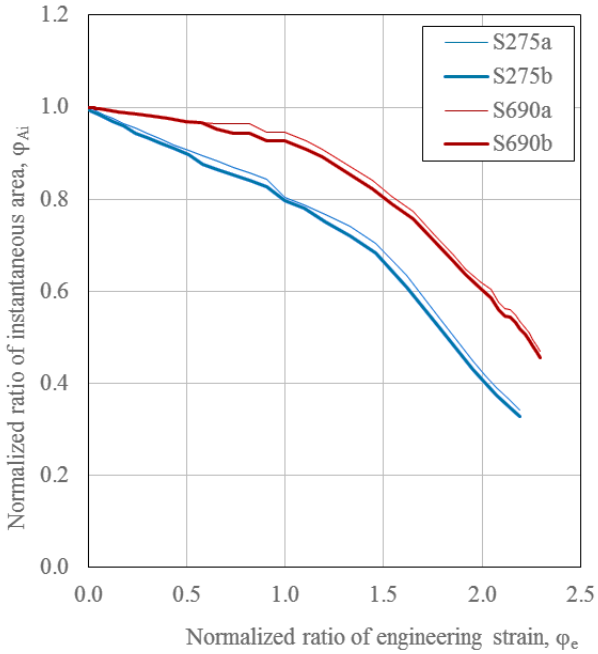

b) Variation of normalized ratios of instantaneous area φ_{Ai} against normalized ratios engineering strain φ_ε

Figure 8: Variation of instantaneous area

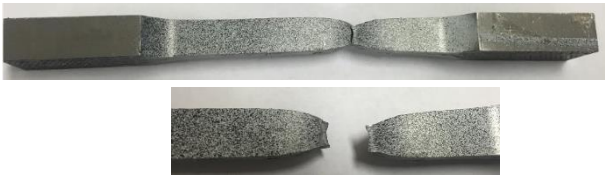

a) Specked surface

b) Surface with strain gauge

Figure 9: Typical failure mode of a S690 steel coupon

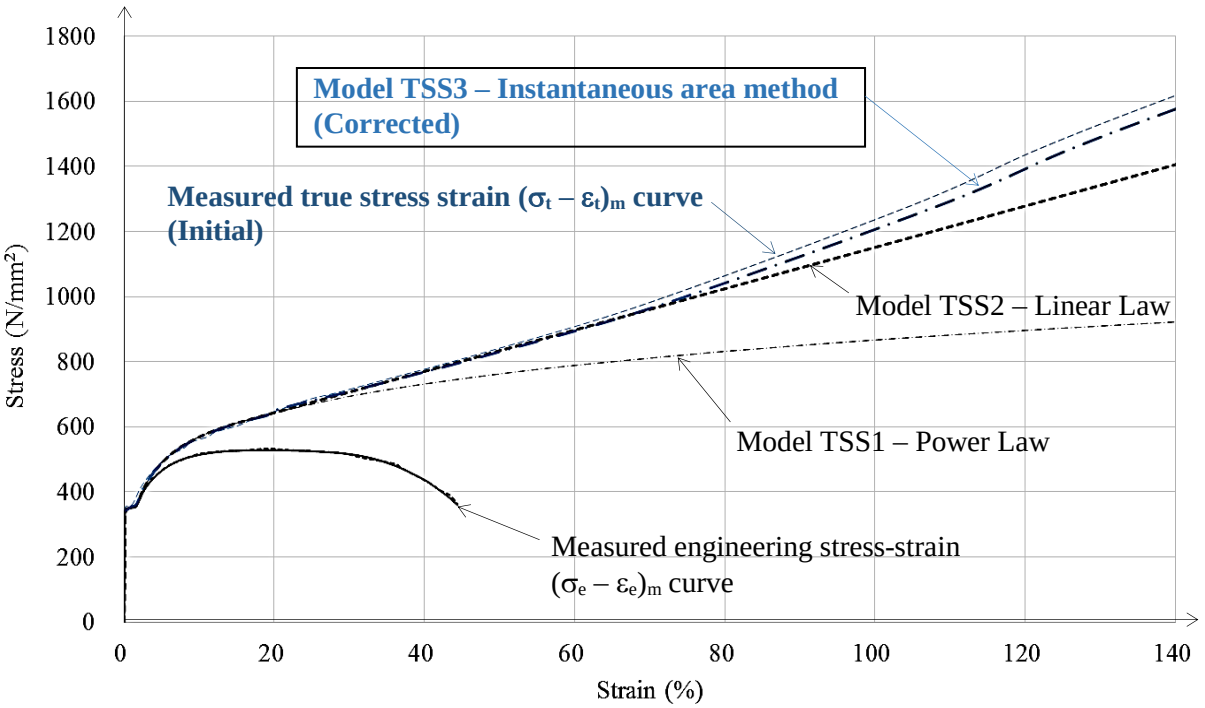

a) S275 steel materials

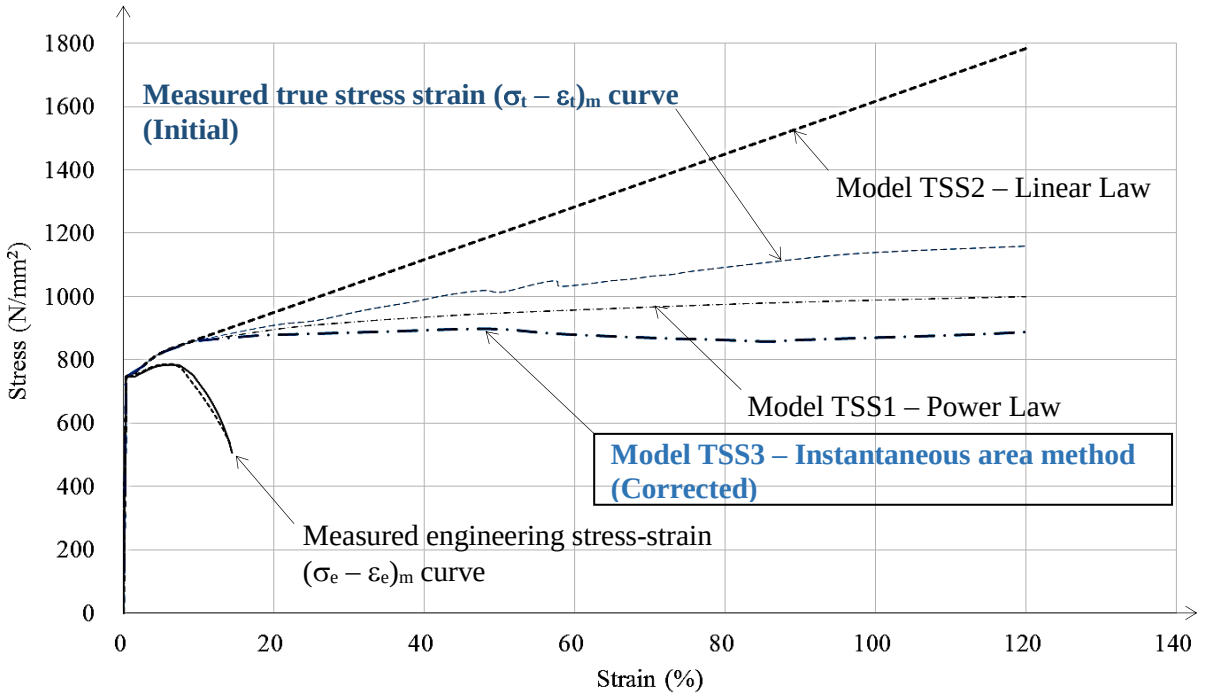

b) S690 steel materials

Figure 10: Engineering stress-strain curves vs true stress-strain curves

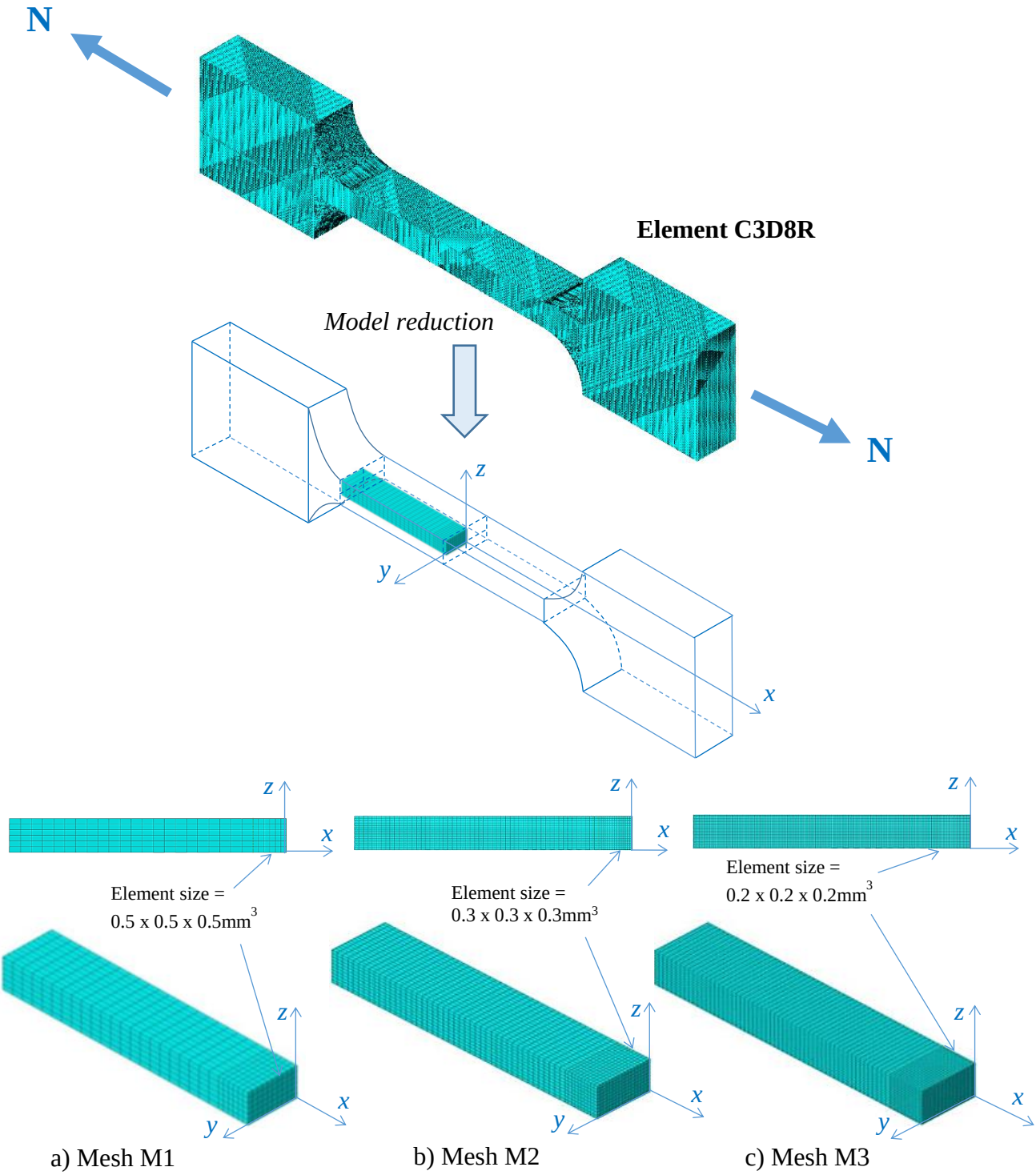

Figure 11: Finite element models with various mesh refinement

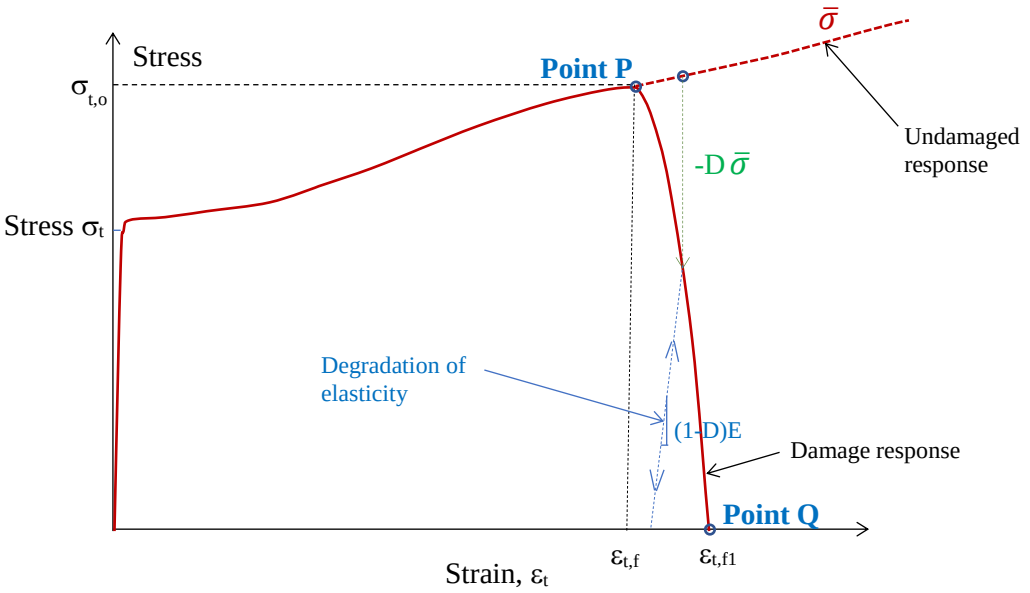

Figure 12: Typical material constitutive behaviour for progressive damage

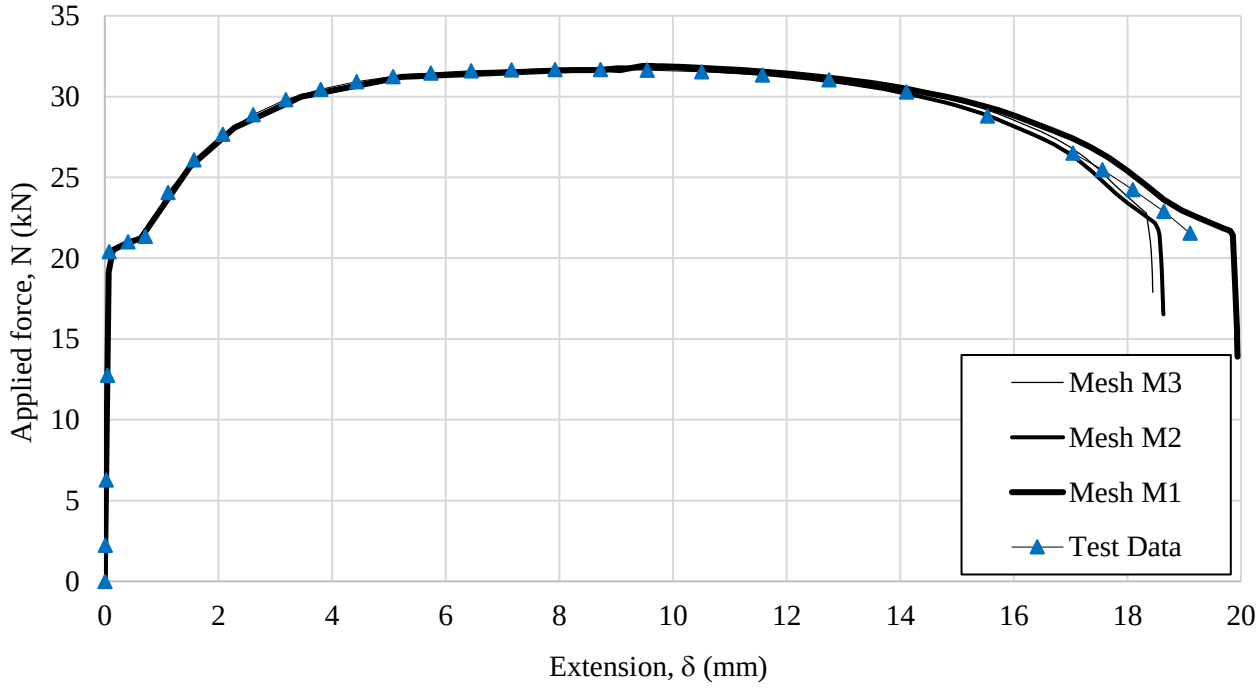

Figure 13: Predicted load-extension curves of various finite element meshes of a S275 steel coupon

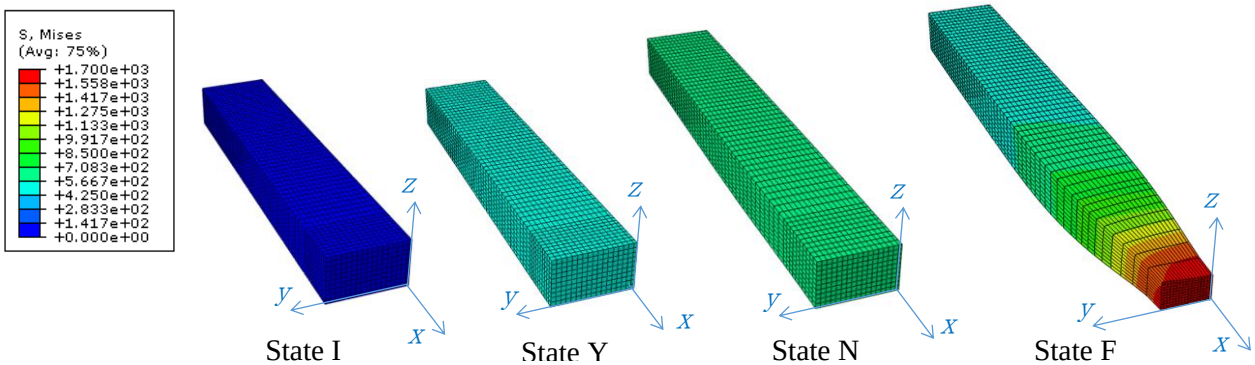

Figure 14: Deformed shape of Mesh M2 at various deformation stages

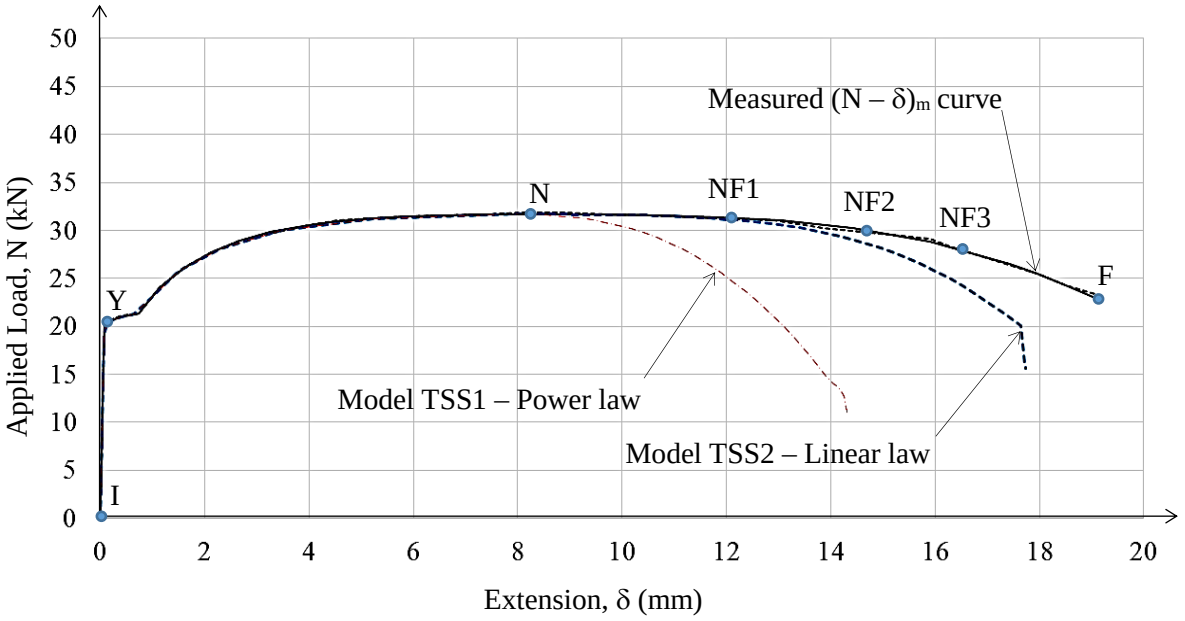

a) S275 steel material

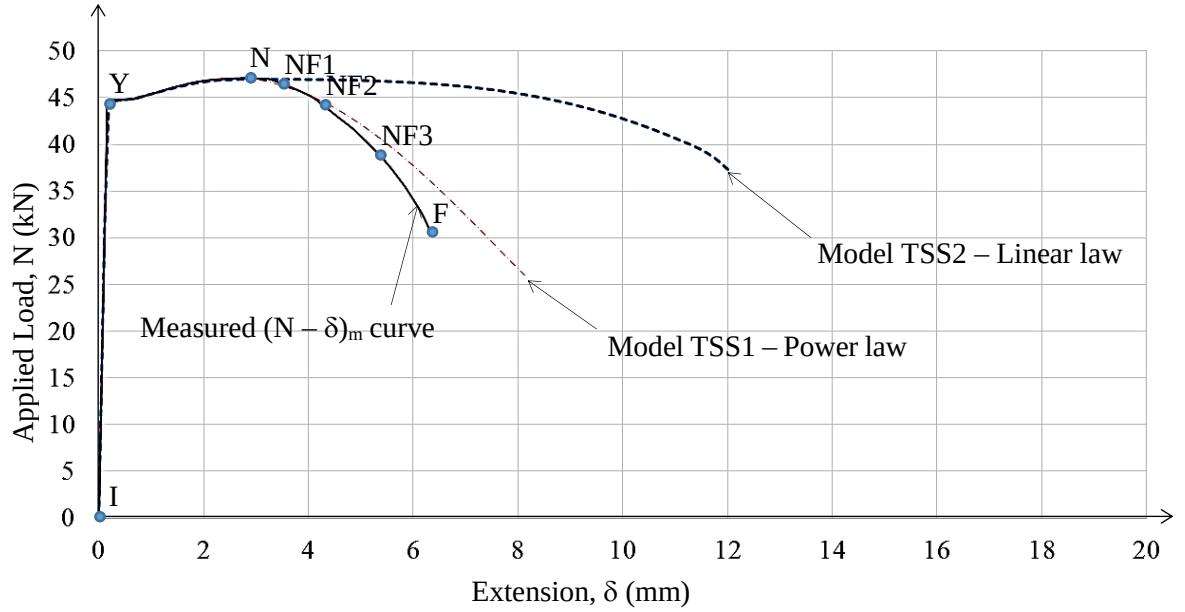

b) S690 steel material

Figure 15: Load-extension curves predicted by finite element models using conventional constitutive formulations

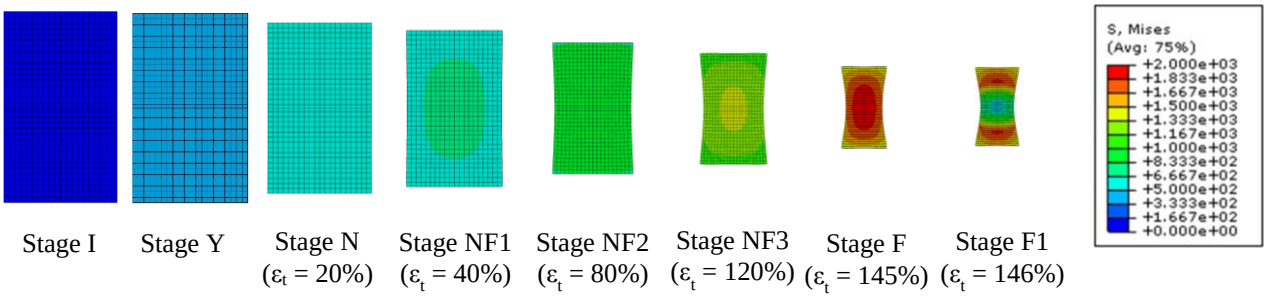

Stage I | Stage Y | Stage N (ε_t = 20%) | Stage NF1 (ε_t = 40%) | Stage NF2 (ε_t = 80%) | Stage NF3 (ε_t = 120%) | Stage F (ε_t = 145%) | Stage F1 (ε_t = 146%)

a) Von Mises stress distributions of the critical cross sections

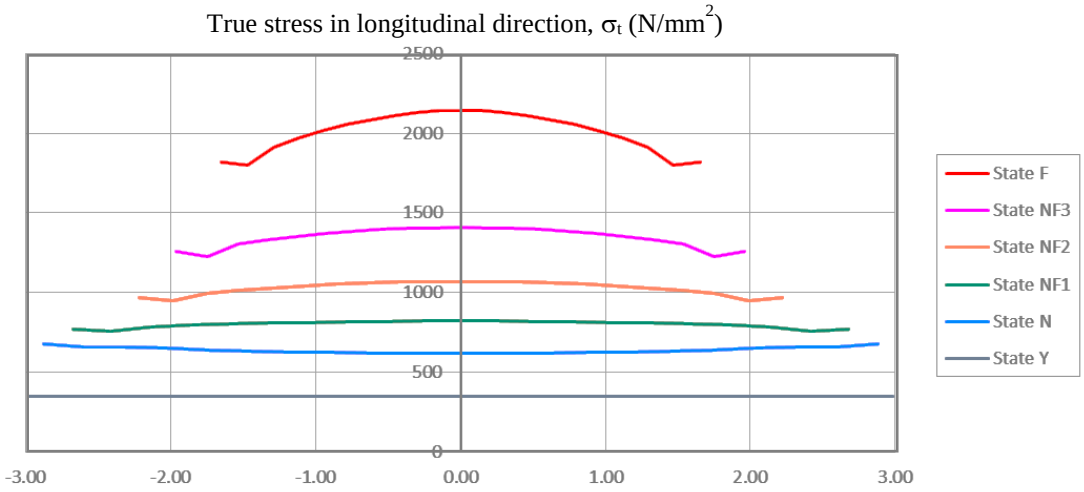

b) Longitudinal stress plots along the mid-line of the critical cross-section

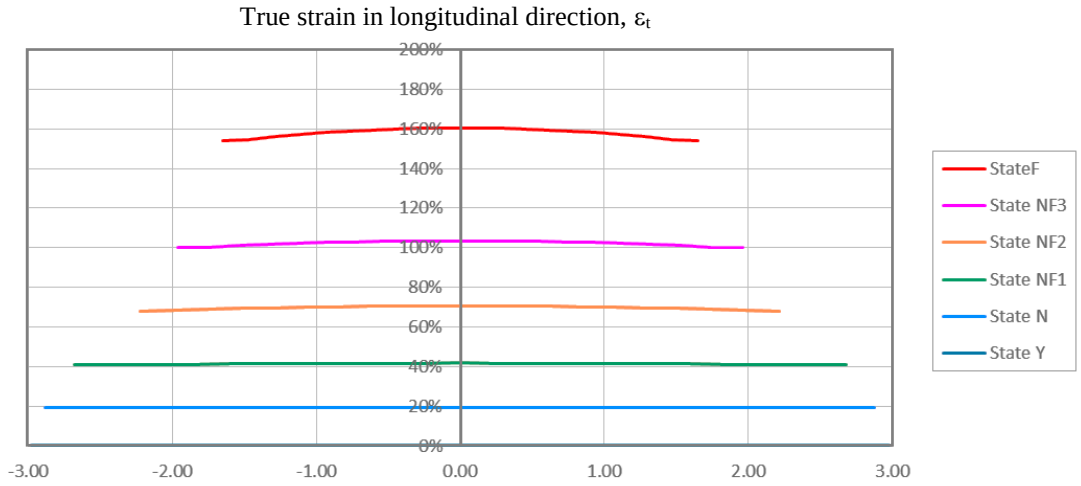

c) Longitudinal strain plots along the mid-line of the critical cross-section

Figure 16: Variations of stress and strain distributions across the critical cross-section at various strain levels of a S275 test coupon

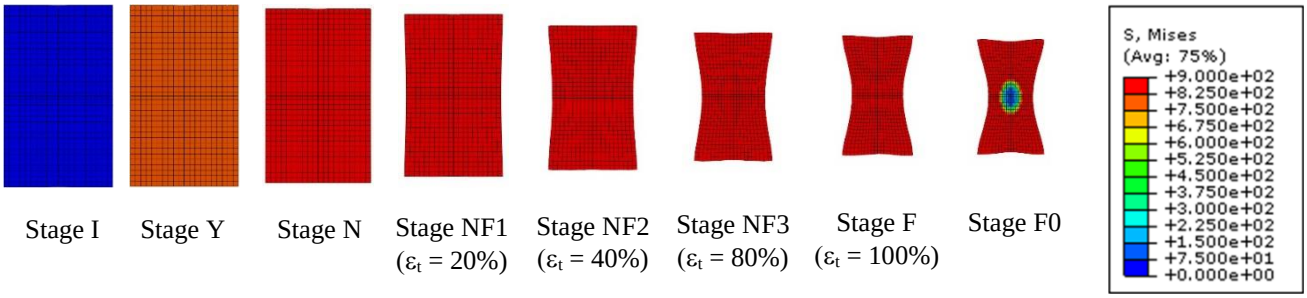

Stage I | Stage Y | Stage N | Stage NF1 (ε_t = 20%) | Stage NF2 (ε_t = 40%) | Stage NF3 (ε_t = 80%) | Stage F (ε_t = 100%) | Stage F0

a) Von Mises stress distributions of the critical cross sections

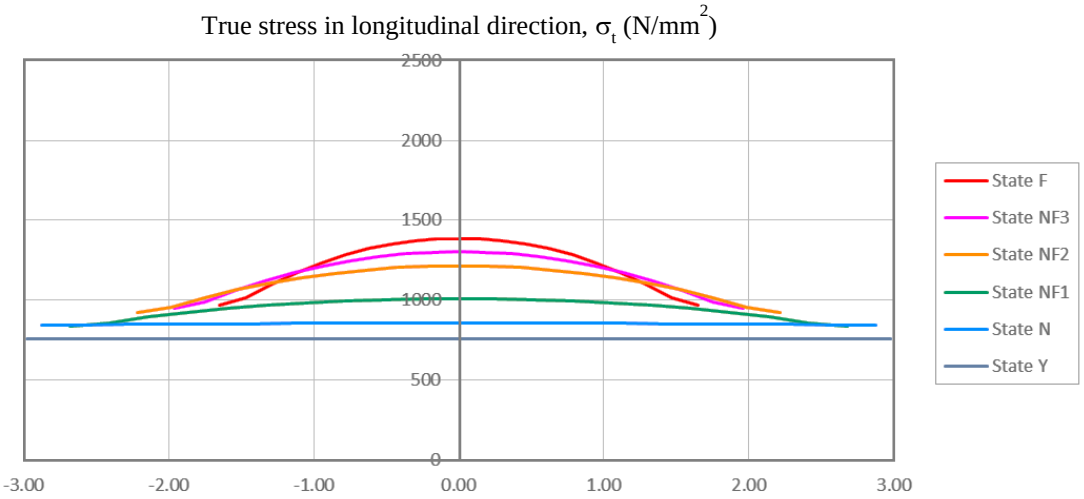

b) Longitudinal stress plots along the mid-line of the critical cross-section

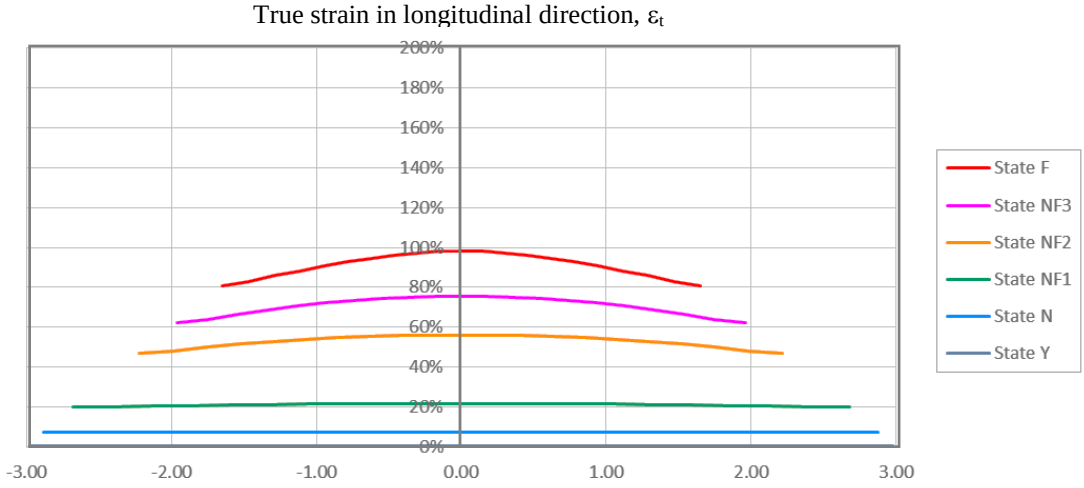

c) Longitudinal true strain plots along the mid-line of the critical cross-section

Figure 17: Variation of stress and strain distributions across the critical cross-section at various strain level of a S690 test coupon

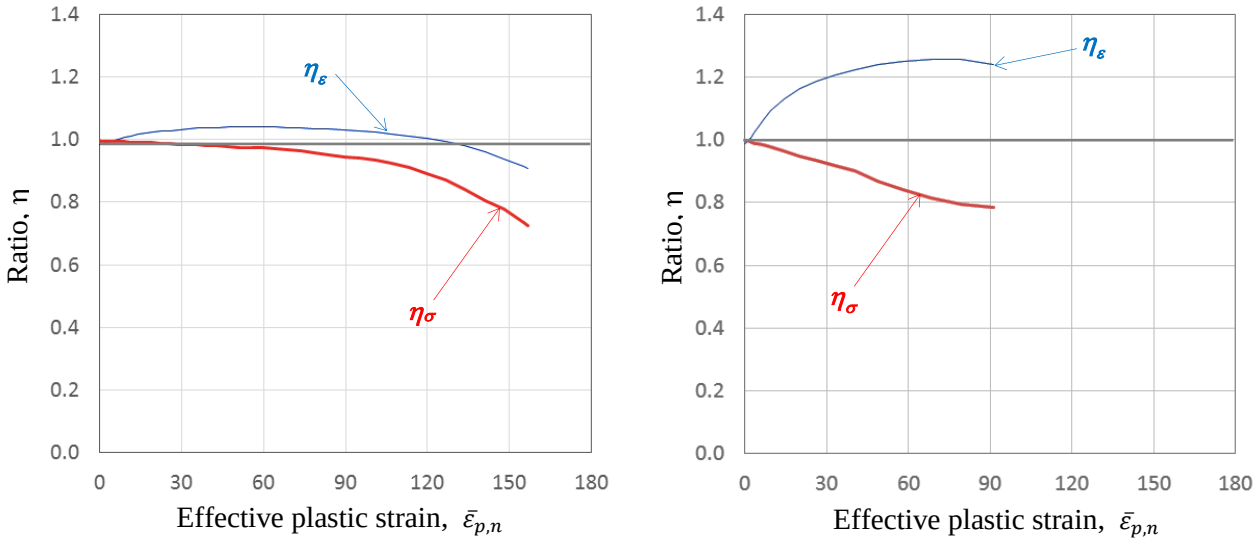

a) Stress and strain correction factors for S275 steel coupons

b) Stress and strain correction factors for S690 steel coupons

*Note: Effective plastic strain after necking, $\bar{\varepsilon}_{p,n}=\varepsilon_p - \varepsilon_{pt}$
where ε_p is plastic strain, and ε_{pt} is the platic strain at tensile strength

Figure 18: Correction factors at various true strains after plastic strains after necking

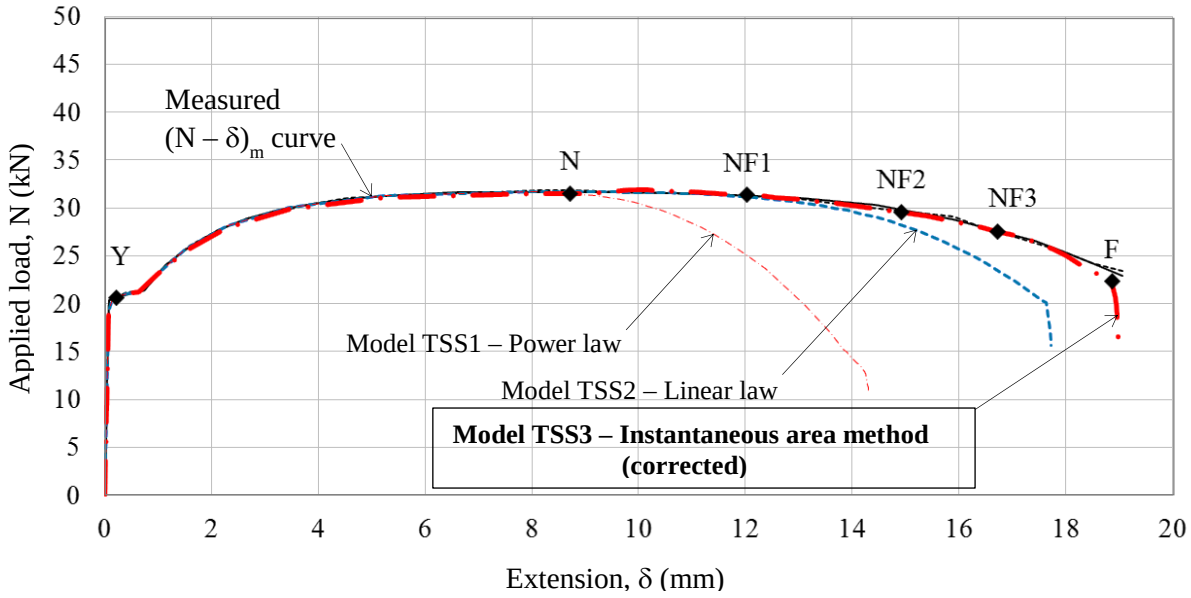

a) S275 coupon

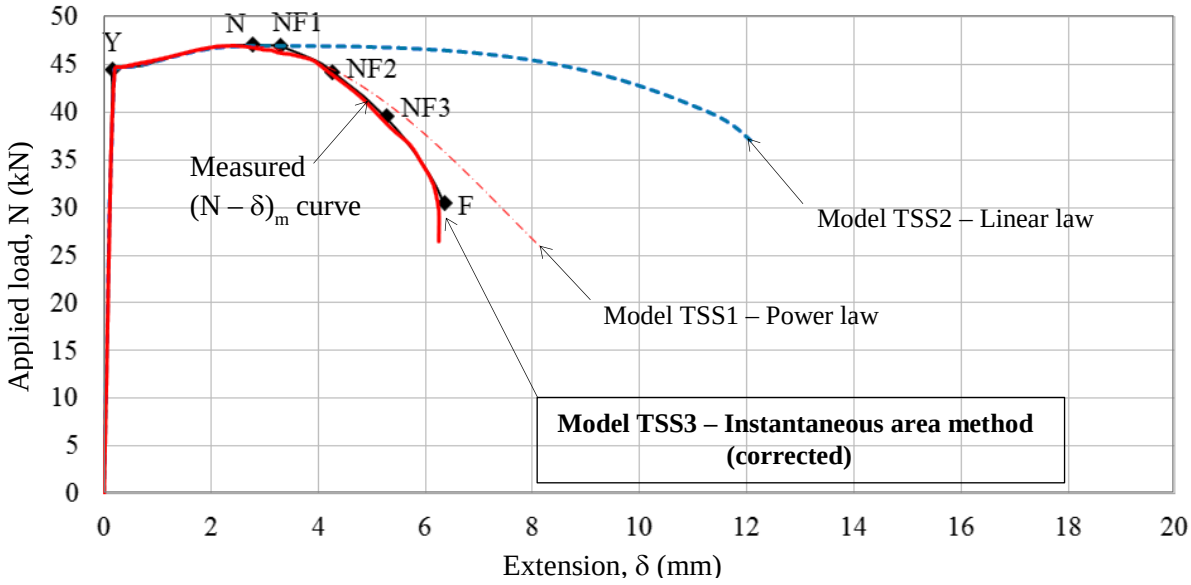

b) S690 coupon

Figure 19: Load-extension $(N - \delta)_p$ curves predicted with various true stress strain ($\sigma_t - \varepsilon_t$) curves.

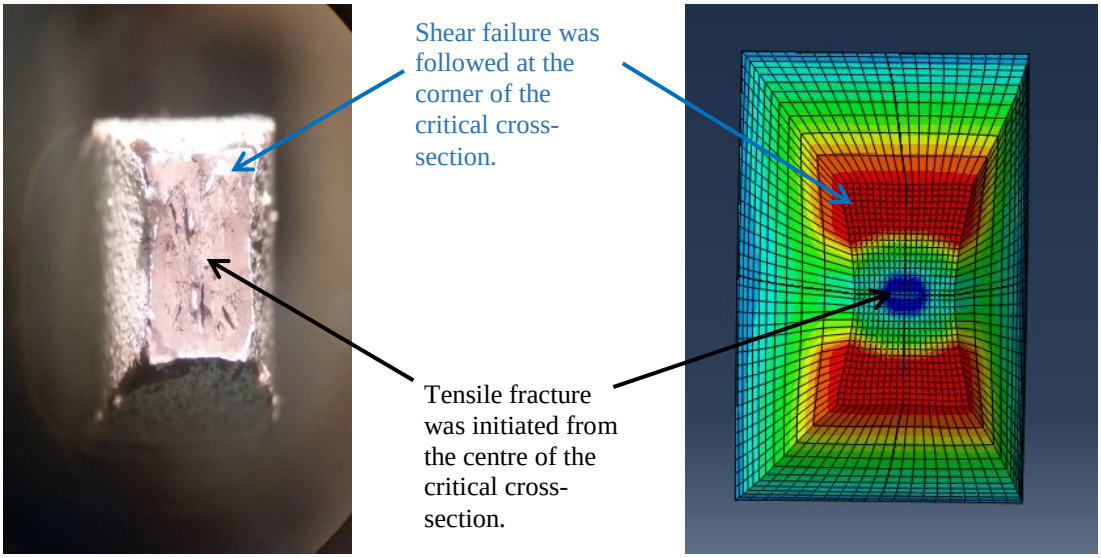

Figure 20: Fractured cross-section of a Q690 tensile coupon

Table 1: Test programme of standard tensile tests

Test specimen	Steel grade	b_o x h_o (mm)
S275-A	S275	10 x 6
S275-B	S275	10 x 6
S690-A	S690	10 x 6
S690-B	S690	10 x 6

Table 2: Test results of standard tensile tests

Test specimen	Steel grade	Nominal dimensions b_o x h_o (mm x mm)	Young's Modulus, E (kN/mm^2)	Yield strength, f_y (N/mm^2)	Tensile strength, f_u (N/mm^2)	Strain at yielding, ε_y (%)	Strain at tensile strength, ε_u (%)	Strain at fracture, ε_L (%)
S275-A	S275	10.0 x 6.00	215	340	528	0.17	20.28	44.42
S275-B	S275	10.0 x 6.00	214	342	531	0.17	20.13	44.28
S690-A	S690	10.0 x 6.00	202	746	780	0.39	6.83	14.51
S690-B	S690	10.0 x 6.00	206	749	787	0.40	5.32	14.37

Table 3: Convergence study on various finite element meshes

Model	Mesh size (mm x mm x mm)	Total number of elements	Maximum applied force $N_{E,R}$ (kN)	Corresponding extension under $N_{E,R}$, (mm)	Elongation at fracture ε_L (%)	Computing time (minutes)
Mesh M1	0.5 x 0.5 x 0.5	1680	14.93	5.99	46.6	34
Mesh M2	0.3 x 0.3 x 0.3	9180	14.92	6.00	42.9	133
Mesh M3	0.2 x 0.2 x 0.2	26250	14.92	6.00	42.5	523

Table 4: Stress correction factors of the finite element models of the standard tensile test for S275 steel coupons

Point	Description	H (mm)	B (mm)	Area (mm^2)	Applied force, N (kN)	True stress, σ_t (N/mm^2)		Stress correction factor,	True Strain, ε_t (%)		Strain correction factor,
						Max. $\sigma_{vm,max}$	Average σ_{av}	η_σ	Principal ε_p	Average ε_{av}	η_ε
Y	Yield	9.98	6.00	59.88	20.5	343.7	342.4	1.003	0.17	0.17	1.000
N	Necking	9.07	5.40	49.02	31.5	640.2	642.3	0.997	19.3	19.4	0.995
NF1	Large deformation	-	-	39.69	31.3	780.7	789.4	0.989	41.8	40.8	1.025
NF2		-	-	26.62	29.6	1078.8	1110.4	0.972	83.4	80.7	1.035
NF3		-	-	18.36	27.6	1403.5	1501.0	0.935	120.5	117.8	1.023
F	Fracture	-	-	8.55	22.3	1892.2	2610.2	0.724	176.1	193.5	0.910

Table 5: Stress correction factors of the finite element models of the standard tensile test for S690 steel coupons

Point	Description	H (mm)	B (mm)	Area (mm^2)	Applied force, N (kN)	True stress, σ_t (N/mm^2)		Stress correction factor,	True Strain, ε_t (%)		Strain correction factor,
						Max. $\sigma_{vm,max}$	Average σ_{av}	η_σ	Principal ε_p	Average ε_{av}	η_ε
Y	Yield	9.99	5.98	59.29	44.8	751.8	754.8	0.996	0.37	0.37	1.000
N	Necking	9.84	5.78	55.40	47.1	846.3	849.5	0.996	7.31	7.40	0.989
NF1	Large deformation	-	-	49.20	45.0	881.9	915.4	0.963	21.83	19.29	1.132
NF2		-	-	42.70	41.6	894.5	973.8	0.919	40.44	33.46	1.209
NF3				32.68	34.7	866.5	1063.0	0.815	79.85	63.88	1.250
F	Fracture	-	-	27.00	30.0	871.9	1112.8	0.784	120.71	100.59	1.200

Table 6: Correction factors in various iterations for modelling of S275 steel coupons

		1st Iteration		2nd Iteration		3rd Iteration		4th Iteration		5th Iteration	
Point	Description	η_σ	η_ε	η_σ	η_ε	η_σ	η_ε	η_σ	η_ε	η_σ	η_ε
Y	Yield	1.003	1.000	1.003	1.000	1.003	1.000	1.003	1.000	1.003	1.000
N	Necking	1.000	0.998	0.999	0.997	0.998	0.996	0.997	0.995	0.997	0.995
NF1	Large deformation	0.998	1.004	0.993	1.021	0.991	1.03	0.989	1.025	0.989	1.025
NF2		0.989	1.004	0.987	1.024	0.972	1.04	0.972	1.035	0.972	1.035
NF3		0.964	1.042	0.966	1.022	0.942	1.02	0.935	1.023	0.935	1.023
F	Fracture	0.891	1.021	0.852	0.971	0.743	0.920	0.725	0.911	0.724	0.910

*Note: - η_σ is the stress correction factor as defined in Section 3.4.
- η_ε is the stress correction factor as defined in Section 3.4.

Table 7: Correction factors in various iterations for modelling of S690 steel coupons

		1st Iteration		2nd Iteration		3rd Iteration		4th Iteration	
Point	Description	η_σ	η_ε	η_σ	η_ε	η_σ	η_ε	η_σ	η_ε
Y	Yield	0.999	1.000	0.997	1.000	0.996	1.000	0.996	1.000
N	Necking	0.999	0.998	0.997	0.992	0.996	0.989	0.996	0.989
NF1	Between	0.982	1.076	0.971	1.115	0.963	1.132	0.963	1.132
NF2	Necking and	0.943	1.173	0.930	1.201	0.919	1.209	0.919	1.209
NF3	Fracture	0.822	1.231	0.818	1.235	0.816	1.248	0.815	1.250
F	Fracture	0.802	1.220	0.793	1.209	0.785	1.202	0.784	1.200

*Note: - η_σ is the stress correction factor as defined in Section 3.4.
- η_ε is the stress correction factor as defined in Section 3.4.